



## **ABSTRACT**

The purpose of this research is to study the fluid dynamics of the dense region of impinging jet atomizers using a novel holographic technique which is able to penetrate this region and to record reliably the non-spherical liquid elements which populate it. During the second year of the research significant progress was made in the study of both low and high speed impingement. The effect of several parameters such as the impingement angle, the liquid jet velocity, and the orifice diameter on the atomization process was investigated. It was shown that in the dense spray region the liquid elements were indeed non-spherical. Smaller and faster droplets were generated with larger impingement angles, higher jet velocities, and smaller orifice diameters. The structure of the liquid elements near the jet impact point is indicative of the mechanisms of the disintegration process. The structure of the dense spray region clearly indicated that utilization of automated techniques that assume that the droplets are spherical for measurements in this region is not appropriate. The data from the holography experiments were used to show that the Universal Root - Normal Distribution is successful in describing the dense spray region. In the coming year the work will focus on the effect of fluid properties and environment temperature on the atomization process.

## DESCRIPTION OF ACTIVITIES DURING THE PAST YEAR

### 1. Experiments

#### 1.1 *Impinging Jet Apparatus*

The impinging jet apparatus was described in last year's report. For brevity this description is not repeated herein.

#### 1.2 *Optical System for Hologram Recording*

A detailed description of the optical system and the novel features of the experimental technique was included in the previous annual report. However, an important issue that was settled last year was that of locating accurately the coordinates of the liquid elements in the domain of the spray in order to produce quantitative results for the droplet size distribution, velocity and concentration (density) in the dense spray region. To this end, in order to find the magnification factor and identify the droplet position, an additional hologram of a grid object was obtained just after fabricating the spray hologram without modifications in the optical system. The grid with numbered horizontal and vertical lines at 5.0 mm intervals was drawn by a computer, copied onto a transparent sheet and attached to a transparent glass plate.

#### 1.3 *Hologram Reconstruction and Image Processing System*

The holograms were reconstructed using a 10 mW He-Ne laser. The reference wave was expanded up to 20 mm diameter by a beam expander and converted to a spherical diverging wave by a plano-concave lens, the same as at recording. The reconstructed virtual image of the droplet was magnified by a Questar telescope macro lens system ( long distance microscope ). A camera which was attached to the end of this system recorded the magnified microscopic images of the liquid droplets. Seven different locations around the liquid sheet were monitored for both pulses. The observation area at each location was approximately  $2.0\text{ cm} \times 2.0\text{ cm}$ . At each location, the droplet images and the grid were photographed. The droplet images were magnified fourfold in the final photographic print ( $7.5\text{ cm} \times 11.0\text{ cm}$ ).

The photographed images were recorded by a CCD camera and inputted to a personal computer for the image analysis. Image Analyst provided by Automatrix Inc. was used as the image processing software. The values of the magnification factor at each location ranged from  $40.0\ \mu\text{m}$  to  $45.0\ \mu\text{m}$  per one pixel of the screen. The diameters of the droplets were obtained by measuring the total area of droplets and calculating the equivalent diameter corresponding to the total area. To measure the horizontal and vertical velocities of droplets, the absolute coordinates of the centroid of the droplets from the origin of the grid for both pulses were measured. Next, the difference in the coordinates of the centroid in each direction between two pulses was divided by the pulse separation time. To verify the accuracy of the diameter measurements, the hologram of a  $4.76\ \text{mm}$  precision steel ball was fabricated and the diameter of this steel ball was measured. The measurement results showed that the error in diameter measurement was less than four percent. The average error for the velocity measurements was estimated to be approximately fifteen percent.

## **2. Results**

Experiments were performed both at low and at high jet impingement velocities. The low speed impingement experiments served to test existing theories. The high speed impingement experiments represent realistic atomization conditions in rocket propulsion.

### **2.1 Results for Low Speed Impingement**

The shapes of the liquid sheet at three different impingement angles are compared with the theoretically predicted shapes in Figure 1. The dotted shapes (corresponding to the outline of the photographed liquid sheet) match rather well with the theoretical predictions of Ibrahim and Przekwas [1] for all impingement angles examined. The only noticeable difference appears at  $\phi = 180^\circ$ . A "V" shape is observed in the theoretical prediction above the impingement point (denoted with a dark circle) as the impingement angle increases. No such shape was visually observed in the experiments (note that the

physical presence of the glass tubes prohibit the photographic recording of the liquid sheet in the neighborhood of  $\phi=180^\circ$ ). As expected, the maximum width of the liquid sheet increases with increasing the impingement angle. However, the maximum length of the liquid sheet is considerably less sensitive to the value of the impingement angle in the range from  $2\theta = 90^\circ$  to  $2\theta = 180^\circ$ . The streaklines due to the movement of droplets (not shown herein) indicated that the droplets are shedding from the edge of the liquid sheet in the tangential direction along the edge instead of moving in the radial direction. This fact is also verified by the measurement of droplet velocities, which will be described later.

The quantitative comparison of the maximum width and the maximum length of the liquid sheet between experimental measurements and theoretical predictions is shown in Fig. 2. The theoretically predicted values of the maximum width [1] in Fig. 2 (a) at low jet impingement velocities match very well with the measured values. However, the theory overestimates the maximum width of the liquid sheet as the jet velocity is increased up to  $V_j = 2.5$  m/s. The disagreement becomes greater at higher velocities, around  $V_j = 3.0$  m/s, especially for  $2\theta=90^\circ$ . The experiments agree with the predicted trend that the dependence of the maximum width of the sheet on the jet impingement velocity is stronger for high impingement angles. The predicted maximum length of the liquid sheet agrees reasonably with the measured values even though the theory underestimates at low jet velocities and overestimates at high jet velocities the experiments (Fig. 2 (b)). The theory predicts practically no difference in the maximum length between  $2\theta = 90^\circ$  and  $2\theta = 120^\circ$ . The experiments support this trend which implies that after a certain impingement angle the shape of the liquid sheet keeps widening while its length remains practically constant.

Figure 3 shows typical photographs of microscopic views of a hologram illustrating the droplet formation process. Figure 3 (a) is a view of a portion of the side of the sheet while Fig.3 (b) is nearly under the bottom (tip) of the sheet ( $\phi = 0^\circ$ ). Two facts are clear: First, there is a great variation in droplet size and second the majority of the droplets features non- spherical shapes in particular in the region underneath the sheet (Fig.3 (b)).

The droplet size measurements are compared to the theoretical predictions of Hasson and Peck [2] as well as Ibrahim and Przekwas [1] in Fig. 4. Note that all the droplets observed were sized and are included in Fig. 4. For all impingement angles (Figs. 4a to 4c), no droplets were observed in the upper region of the liquid sheet ( $\phi > \pm 90^\circ$ ) due to the shedding mechanism of droplets in the tangential direction. On the other hand, the theories predicted the existence of droplets all around the liquid sheet because they relied on the assumption that droplets are disintegrating at all locations around the edge of the liquid sheet moving in the radial direction. The predicted droplet size distribution using Hasson and Peck's expression [2] for the thickness of the liquid sheet is similar to that obtained using Ibrahim and Przekwas's expression [1]. In general, the predicted size distribution falls within the range of the measured values. However, the theories fail to account for the wide distribution of droplet sizes ranging from  $500 \mu\text{m}$  up to  $3000 \mu\text{m}$ . This discrepancy comes from the assumption of Dombrowski and Johns [3] that only one size of droplets is created at each angular location from the unstable liquid ligaments. This assumption was adopted by all subsequent studies of the process [1,2,4]. It is recommended that future modeling efforts describe the disintegration of unstable liquid ligaments in a manner that allows for the generation of multiple size of droplets. The co-existence of small and large droplets around small values of  $\phi$  (tip of the liquid sheet) can be physically explained by the likelihood of the presence and partial disintegration of large liquid ligaments in this region. On the other hand, droplets existing at side regions of the liquid sheet (away from the tip) are perhaps more likely to be torn off directly from the edge of the sheet so that their diameters are comparable to the sheet thickness.

Figures 5a and 5b show the horizontal and vertical velocity components of the droplets for two characteristic impingement angles. The horizontal velocities clearly show that droplet shedding occurs tangentially along the edge and not radially. This fact, combined with the cardioid shape of the sheet (Fig. 1) are responsible for the presence of negative horizontal velocities in the right half of the sheet in the vicinity of  $\phi = 0^\circ$  and

positive horizontal velocities in the left half of the sheet in the same vicinity. The vertical velocity components of the droplets show good symmetry with respect to  $\phi = 0^\circ$  with the maximum occurring at  $\phi = 0^\circ$ . The droplets in the vicinity of  $\phi = 0^\circ$  move straight downward.

## 2.2 *Results for High Speed Impingement*

The measurements focused on the determination of the effect of the impingement angle, liquid jet velocity, and orifice diameter on the dense region of the spray. Representative results will be discussed next.

Figure 6 demonstrates the ability of the double pulse holographic technique to record the size and position of liquid elements at two different times for high speed impingement. The region shown is downstream along the spray axis. The droplet identified as no. 1 in Figure 6 (a) corresponding to the first pulse moved to the location identified as no. 1 in Figure 6 (b) corresponding to the second pulse. This photograph also demonstrates the size diversity of the liquid elements as well as the fact that these elements are largely non-spherical. The photographs of the holograms in Figure 7 reveal clearly the disintegration process of the liquid sheet produced by two high-speed impinging jets. The impact wave produced at the impaction point due to the obliquely colliding jets causes the detachment of arc shaped liquid ligament from the liquid sheet as shown in Figure 7 (a). These ligaments progressively disintegrate as they move downstream as shown in Figure 7 (b). Further downstream, Figure 7 (c), only small size droplets are observed. Compared to the droplets in Figure 6, the droplets in Figure 7 are smaller because the impingement angle is increased from  $60^\circ$  in Figure 6 to  $90^\circ$  in Figure 7 with all the other parameters kept unchanged.

Figures 8 and 9 show the effect of the impingement angle, liquid jet velocity, and orifice diameter on the droplet diameter and velocity, respectively. These results were obtained by averaging the measurements for all droplets taken at six different locations. The sampling area in each location was 1.0 cm x 1.5 cm. Figure 8 shows that, in an



average sense, smaller droplets (desirable from the combustion standpoint) were produced with larger impingement angles, higher jet velocities, and smaller orifice diameters. With reference to Figure 9,  $V_x$ ,  $V_y$ , and  $V_m$  indicate the horizontal velocity, the vertical velocity, and the magnitude of the velocity vector, respectively. Increasing the impingement angle or the jet velocity increases the droplet velocity. On the other hand, increasing the jet diameter decreases the droplet velocity. The effect of the aforementioned factors, is considerably stronger on the droplet diameter than it is on the droplet velocity. To exemplify, increasing the jet impingement velocity from 12 m/s to 20 m/s decreases the Sauter Mean Diameter from about 440  $\mu\text{m}$  to about 300  $\mu\text{m}$  (Figure 8). An increase in the jet impingement velocity from 12 m/s to about 15.5 m/s, increased the horizontal component of the mean velocity from about 4 m/s to about 5 m/s (Figure 9).

### 2.3 *Characterization of the Dense Spray Region in High Speed Impingement*

Like most practical atomizers, the impinging jet atomizer does not produce sprays of uniform drop size; instead, the generated drop sizes vary widely. Therefore, in addition to mean drop size, another important parameter to characterize this atomizer is the distribution of drop sizes. The drop size distribution can be represented with a frequency distribution curve or a cumulative distribution curve. The typical ordinates of the frequency distribution curve are the number (or volume) of drops with a given diameter, or the relative number (or volume) of the total. The cumulative distribution representation is essentially a plot of the integral of the frequency curve, and it may represent the percentage of the total number (or surface area, volume) of drops below a given diameter.

Many researchers have attempted to find suitable mathematical or empirical expressions for the drop size distribution in sprays. Examples of distributions in use are the normal, the log-normal, the Nukiyama-Tanasawa, the Rosin-Rammler, and the upper-limit distributions [5]. In the present study the Rosin-Rammler distribution, which is one of the most widely used presently, and the *universal* root-normal distribution proposed by Simmons [6] were compared with the experimental data. Before proceeding with the



results of these comparison a brief background on the abovementioned two distributions is presented

#### *The Rosin-Rammler Distribution*

This distribution may be expressed in the form:

$$1 - Q = \exp \left( -\frac{D}{X} \right)^q \quad (2)$$

where  $Q$  is the fraction of the total volume contained in drops of diameter less than  $D$ ,  $q$  is a size distribution parameter, and  $X$  is a characteristic diameter. The exponent  $q$  provides a measure of the spread of drop sizes. The higher the value of  $q$ , the more uniform the spray is. The values of  $q$  and  $X$  are obtained by plotting eq. (1) in a log-log scale. Solution of the equation  $1-Q = \exp(-1)$  yields the result that  $Q = 0.632$ , which means that  $X$  is the drop diameter such that 63.2% of the total liquid volume is in drops of smaller diameter.

#### *The Universal Root-Normal Distribution*

This distribution is based on the normal distribution of statistics. The customary expression of the normal distribution is

$$f(x) = \frac{1}{\sqrt{2\pi}\sigma} \exp \left[ -\frac{1}{2} (x - \mu)^2 / \sigma^2 \right] \quad (3)$$

where  $\sigma$  is the standard deviation, i.e., the measure of the deviation of the value of  $x$  from a mean value  $\mu$ . The integral of the normal curve is the cumulative function of the normal distribution,  $F(x)$ .

$$F(x) = \int_{-\infty}^x f(x') dx' = \int_{-\infty}^x \frac{1}{\sqrt{2\pi}\sigma} \exp \left[ -\frac{1}{2} (x' - \mu)^2 / \sigma^2 \right] dx' \quad (4)$$

Using the notation

$$t = \frac{x - \mu}{\sqrt{2} \sigma} \quad (5)$$

it can be shown that  $F(x)$  can be expressed in terms of the error function

$$\begin{aligned} F(t) &= \frac{1}{\sqrt{\pi}} \int_{-\infty}^t \exp^{-t'^2} dt' = \frac{1}{2} \left\{ \frac{2}{\sqrt{\pi}} \int_{-\infty}^t \exp^{-t'^2} dt' \right\} \\ &= \frac{1}{2} \{ 1.0 + \operatorname{erf}(t) \} \end{aligned} \quad (6)$$

Simmons [6] showed that a universal nondimensional correlation can be established for various sprays regardless of nozzle type and fuel viscosity, when the drop diameter is normalized to the MMD of the spray and plotted against the cumulative volume percentage. Hence, the variable  $x$  in eq. (5) is replaced by  $\sqrt{\frac{D}{D_{MMD}}}$ . The value of  $\mu$  is 1.0 by definition and that of  $\sigma$  is 0.238, determined graphically. Thus, given only the MMD, it is possible to predict the cumulative volume distribution using eq. (6) for any nozzle and operating condition.

Figures 10 to 15 show that while the Rosin-Rammler distribution describes the droplet distribution in the spray only approximately in most cases, the universal root-normal distribution performs very well considering the complexity of the dense spray region. This is true for all three impingement angles examined (Figs. 10 12). The performance of the universal root-normal distribution continues to be very good when the jet impingement velocity is increased from 12m/s in Fig. 10 to 15.4m/s in Fig. 13 and to 19.1m/s in Fig. 14. Finally the universal root-normal distribution also performs very well when the jet diameter is increased from 1mm in Fig. 10 to 1.5mm in Fig. 15.

**Acknowledgment**

We would like to thank Professor G.M. Faeth of the University of Michigan for bringing to our attention the Universal Root-Normal Distribution proposed by Simmons [4].

## References

1. E. A. Ibrahim and A. J. Przekwas, Impinging Jets Atomization, *Physics of Fluids A*, vol. 3, pp. 2981 - 2987, 1991.
2. D. Hasson and R. E. Peck, Thickness Distribution in a Sheet Formed by Impinging Jets, *A.I.Ch.E. Journal*, vol. 10, pp. 752 - 754, 1964.
3. N. Dombrowski and W. R. Johns, The Aerodynamic Instability and Disintegration of Viscous Liquid Sheets, *Chemical Engineering Science*, vol. 18, pp. 203 - 214, 1963.
4. H. S. Couto, D. Bastos-Netto and C. E. Migueis, Modeling of the Initial Droplet Size Distribution Function in the Spray Formed by Impinging Jets, *Journal of Propulsion*, vol. 8, pp. 725 - 728., 1992.
5. A. H. Lefebvre, *Atomization and Sprays*, Hemisphere, N.Y., 1989.
6. H.C. Simmons, The Correlation of Drop-Size Distributions in Fuel Nozzle Sprays, *J. Eng. for Power*, vol.99, pp. 309-319, 1977.

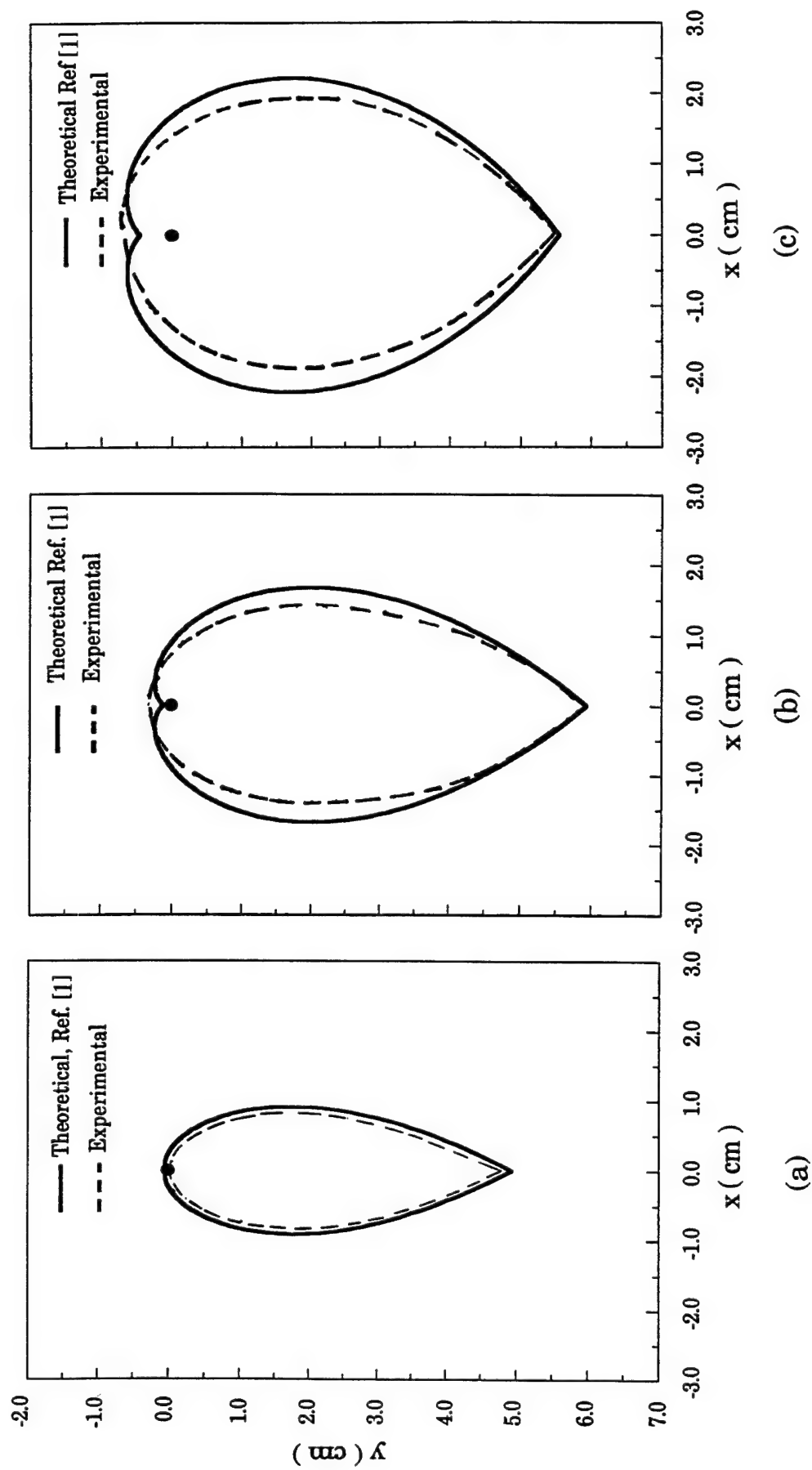


Figure 1 Comparison of the photographed shape of the liquid sheet with the theoretically predicted shape for  $D_j = 1.5 \text{ mm}$ ,  $V_j = 2.49 \text{ m/s}$   
(a)  $2\theta = 60^\circ$  (b)  $2\theta = 90^\circ$  (c)  $2\theta = 120^\circ$ .

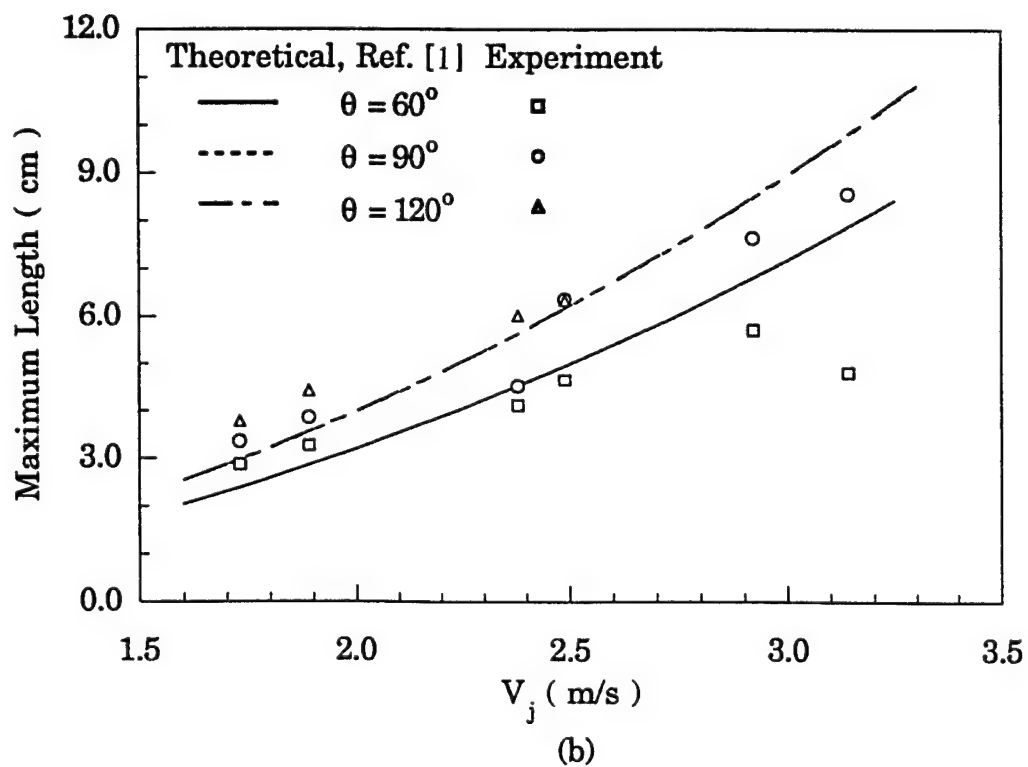
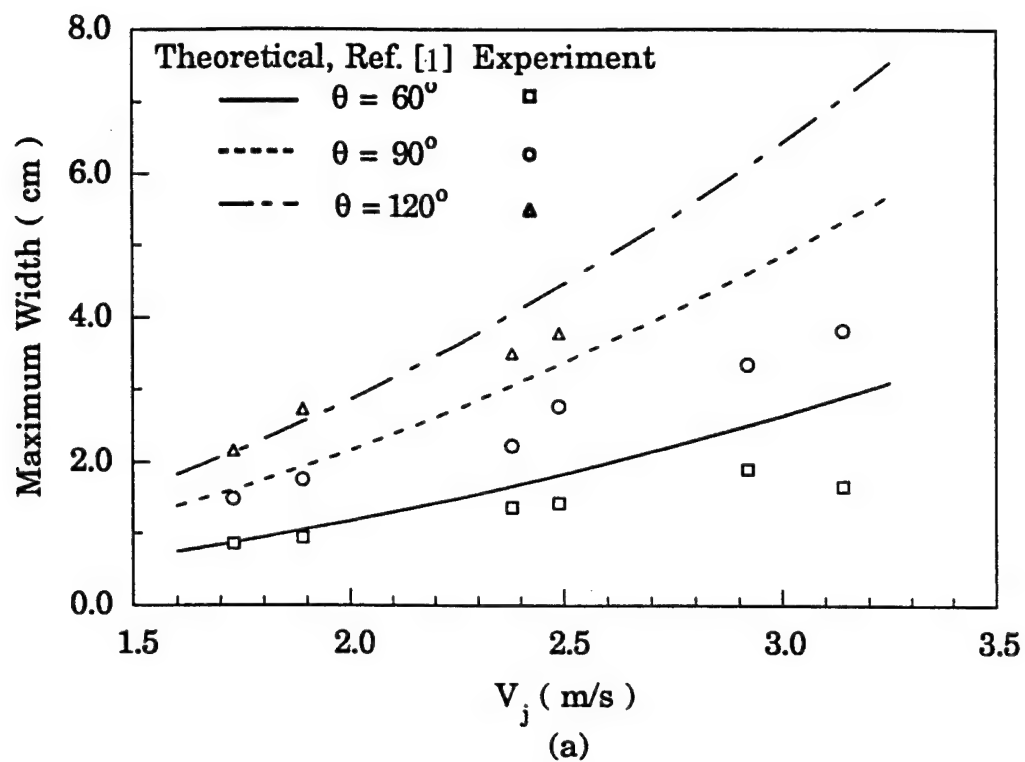
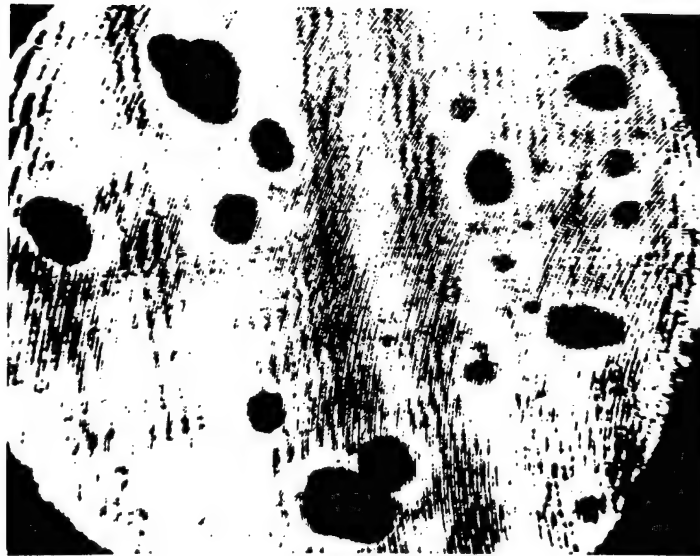


Figure 2 Comparison of the measured maximum width and length of the liquid sheet with theoretically predicted values for  $D_j = 1.5$  mm,  $V_j = 2.49$  m/s (a) maximum width (b) maximum length.



(a)



(b)

Figure 3 Typical photographs of a hologram revealing droplet images at two different locations for  $D_j = 1.5$  mm,  $V_j = 2.49$  m/s,  $2\theta = 120^\circ$  (a) upper right region of the sheet (  $x = 1.6$  to  $3.3$  cm,  $y = -0.5$  to  $2.0$  cm ) (b) lower left region (  $x = -2.5$  to  $-1.0$  cm,  $y = 4.0$  to  $5.7$  cm ).



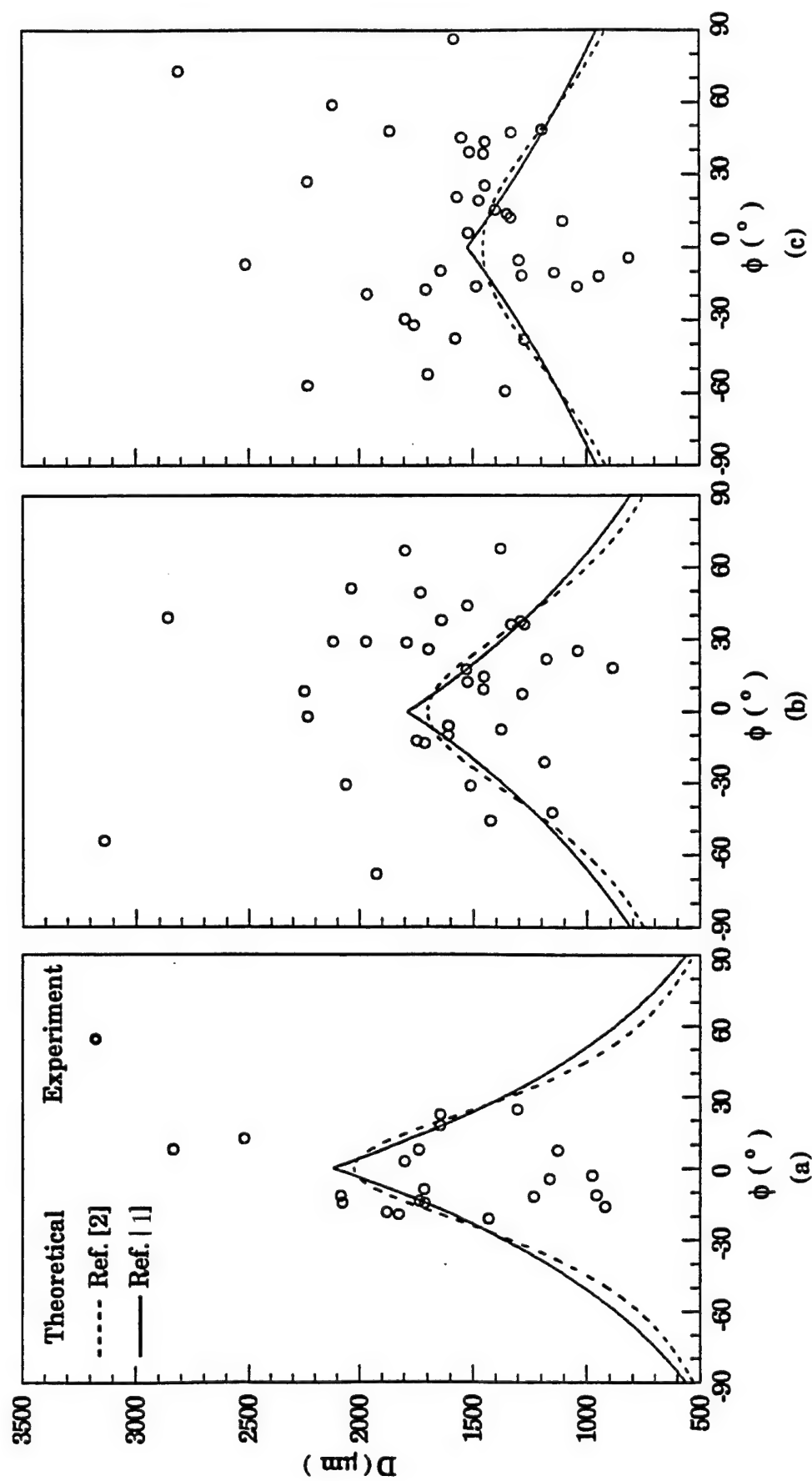


Figure 4 Measured droplet size distribution and comparison with theoretical predictions for  $D_j = 1.5$  mm,  $V_j = 2.5$  m/s  
 (a)  $2\theta = 60^\circ$  (b)  $2\theta = 90^\circ$  (c)  $2\theta = 120^\circ$ .

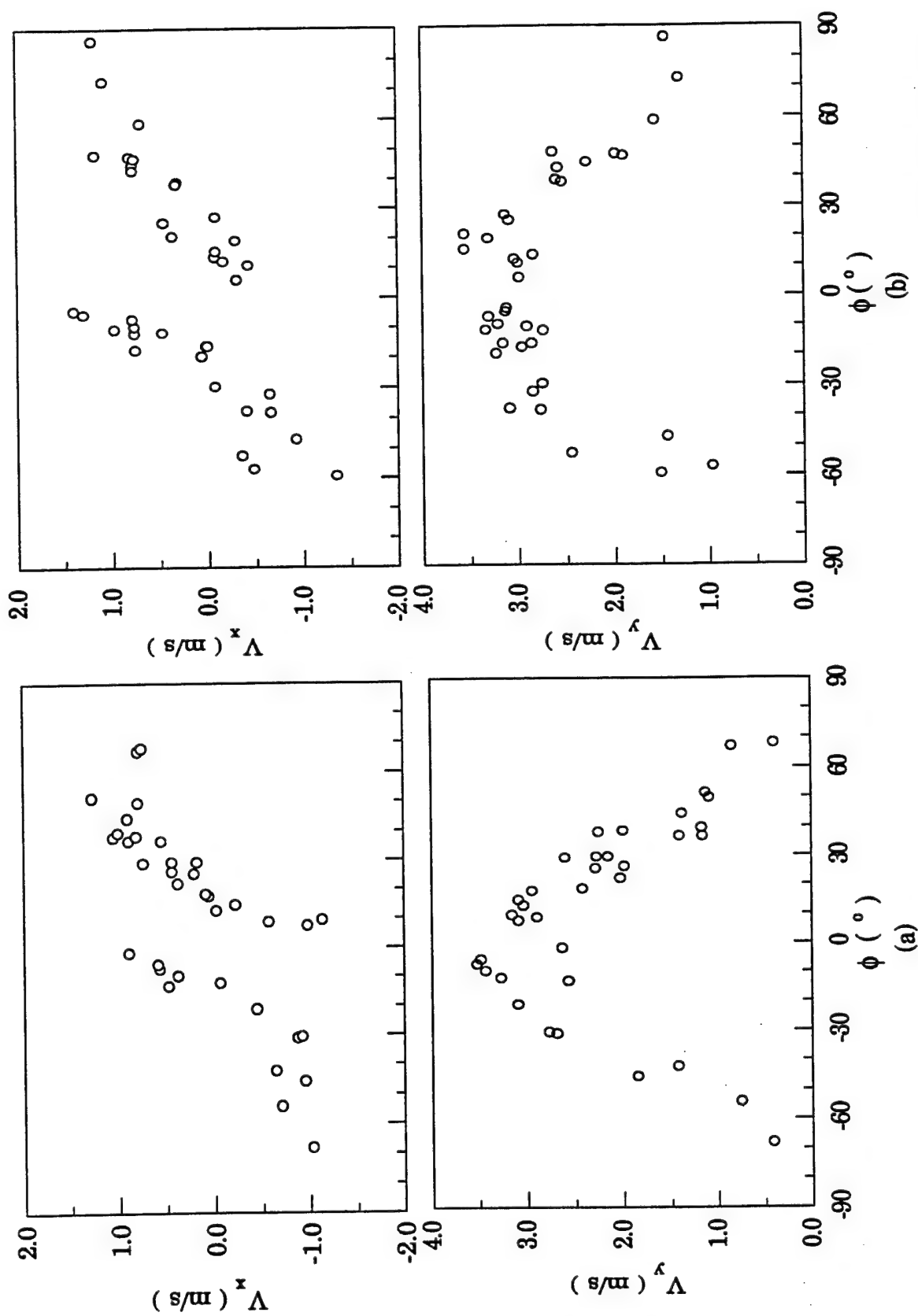


Figure 5 Measured velocity components of the liquid droplets for  $D_j = 1.5$  mm,  $V_j = 2.5$  m/s (a)  $2\theta = 90^\circ$  (b)  $2\theta = 120^\circ$ .

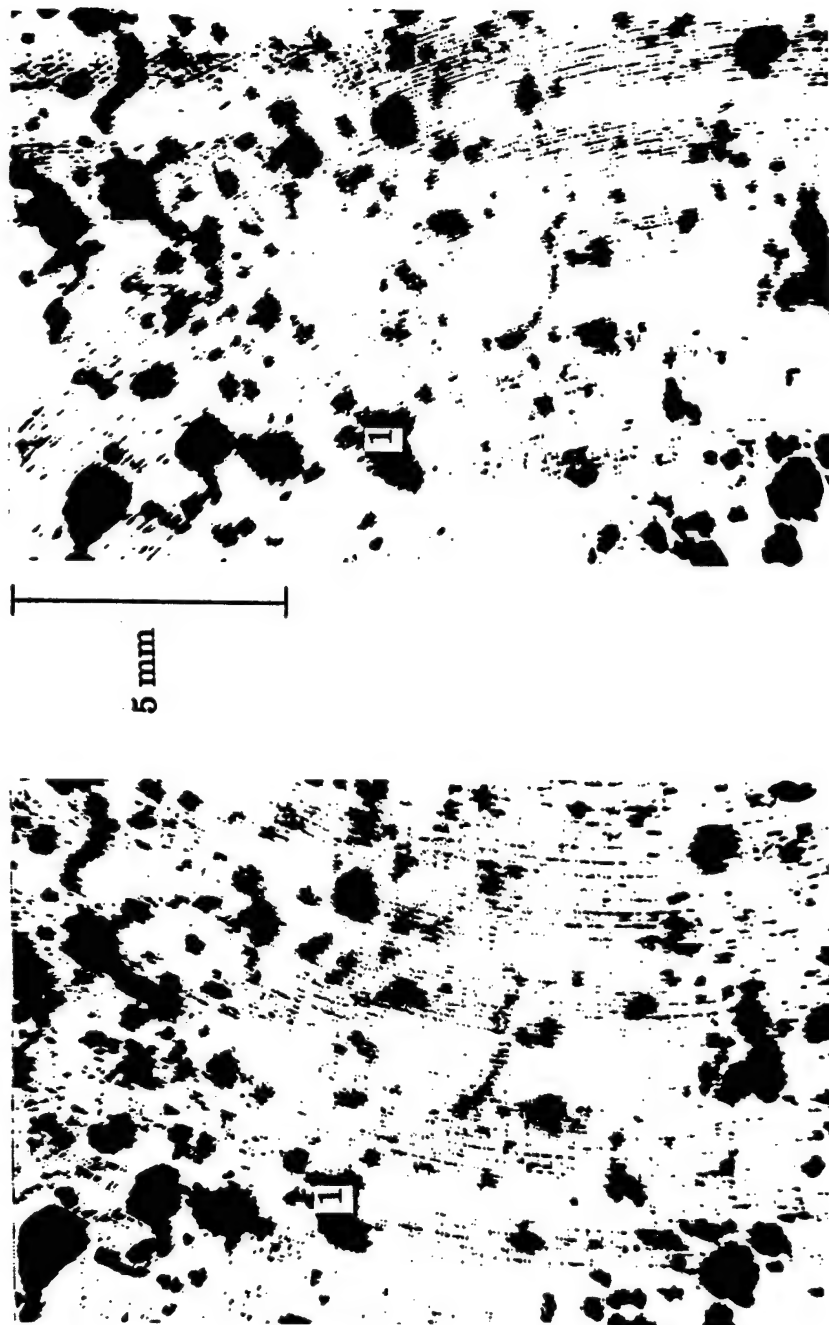
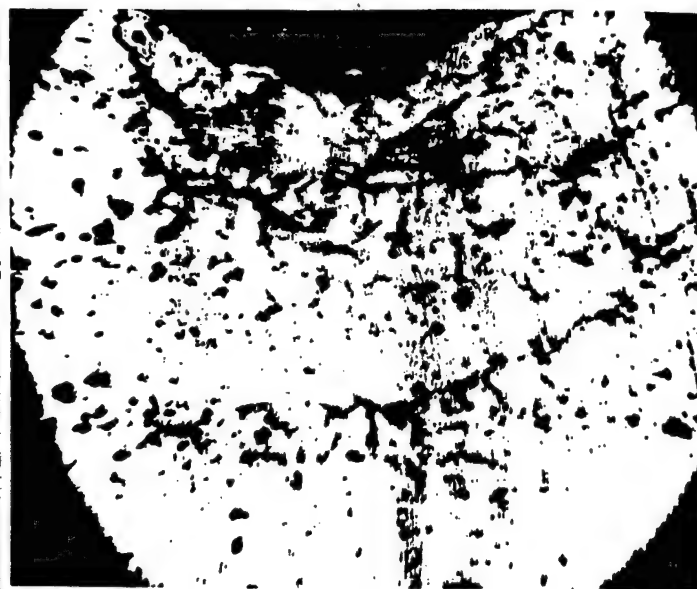


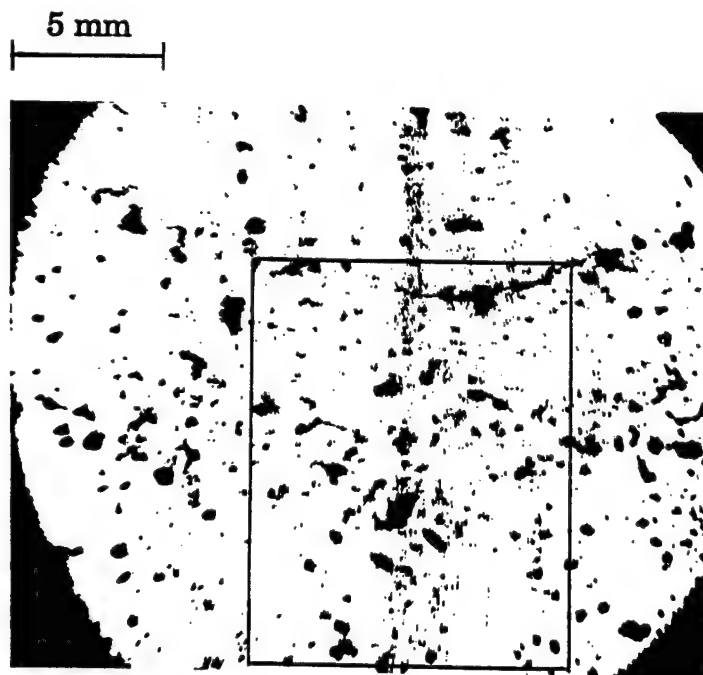
Figure 6 Photographs of hologram revealing droplet images at the first and the second pulse with impingement angle  $2\theta = 120^\circ$ ,  $V_j = 12.0$  m/s,  $D_j = 1.0$  mm,  $(x, y) = (0.0$  cm,  $4.0$  cm) (a) droplet images at the first pulse, (b) droplet images at the second pulse.



y = 0.0 to y = 1.5 cm



y = 1.5 to y = 3.0 cm



y = 3.0 to y = 4.5 cm



5 mm

Figure 7 Photographs of hologram revealing the structure of the sheet disintegration with impingement angle  $2\theta = 90^\circ$ ,  $V_j = 12.0$  m/s,  $D_j = 1.0$  mm (a) y = 0.0 to y = 1.5 cm (b) y = 1.5 to y = 3.0 cm (c) y = 3.0 to y = 4.5 cm (d) microscopic detail of the region identified by a square in Figure 7 (c).

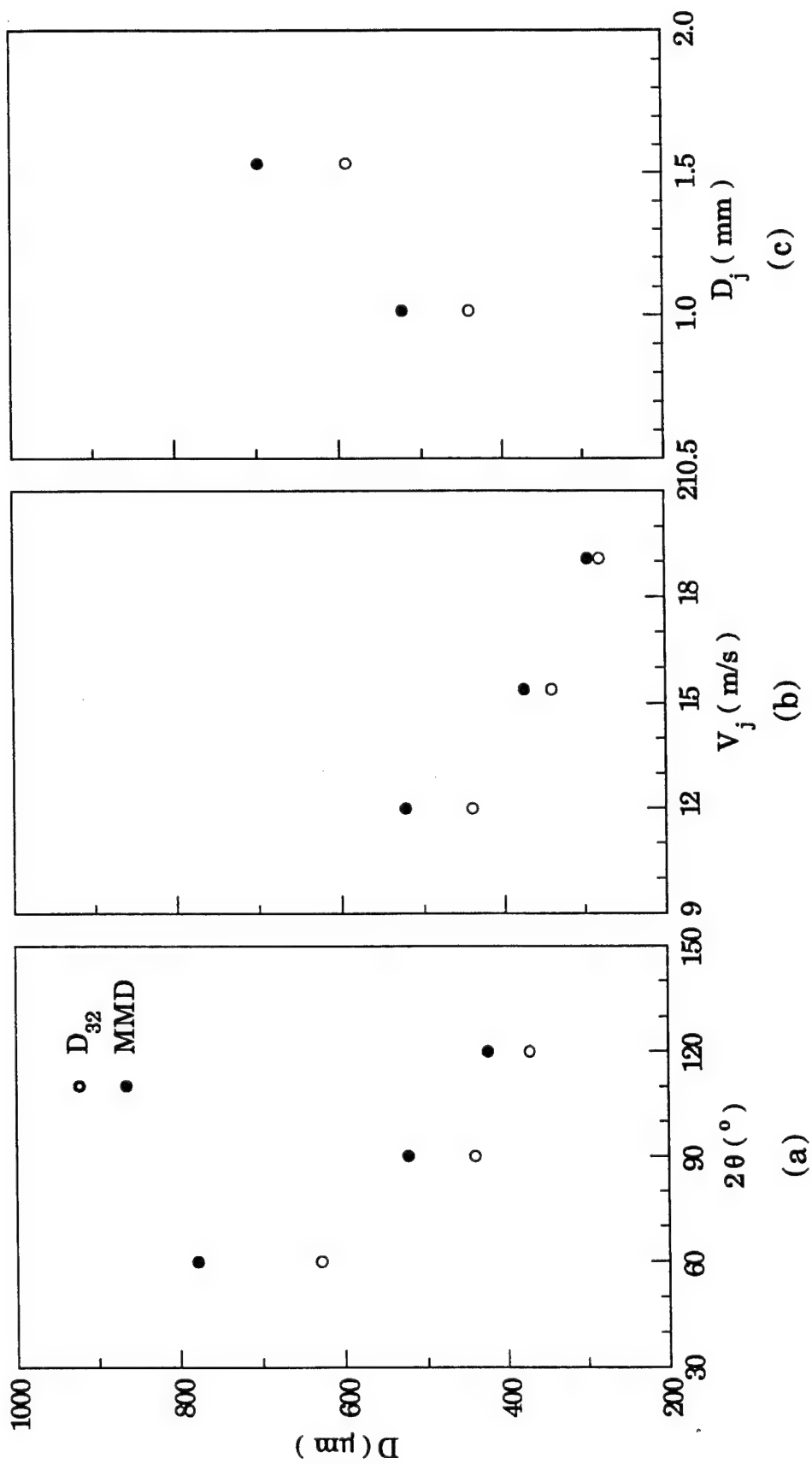


Figure 8 Effect of impingement angle, liquid jet velocity, and orifice diameter on Mean Diameters (a)  $D_j = 1.0$  mm,  $V_j = 12.0$  m/s, (b)  $D_j = 1.0$  mm,  $2\theta = 90^\circ$ , (c)  $V_j = 12.0$  m/s,  $2\theta = 90^\circ$ .

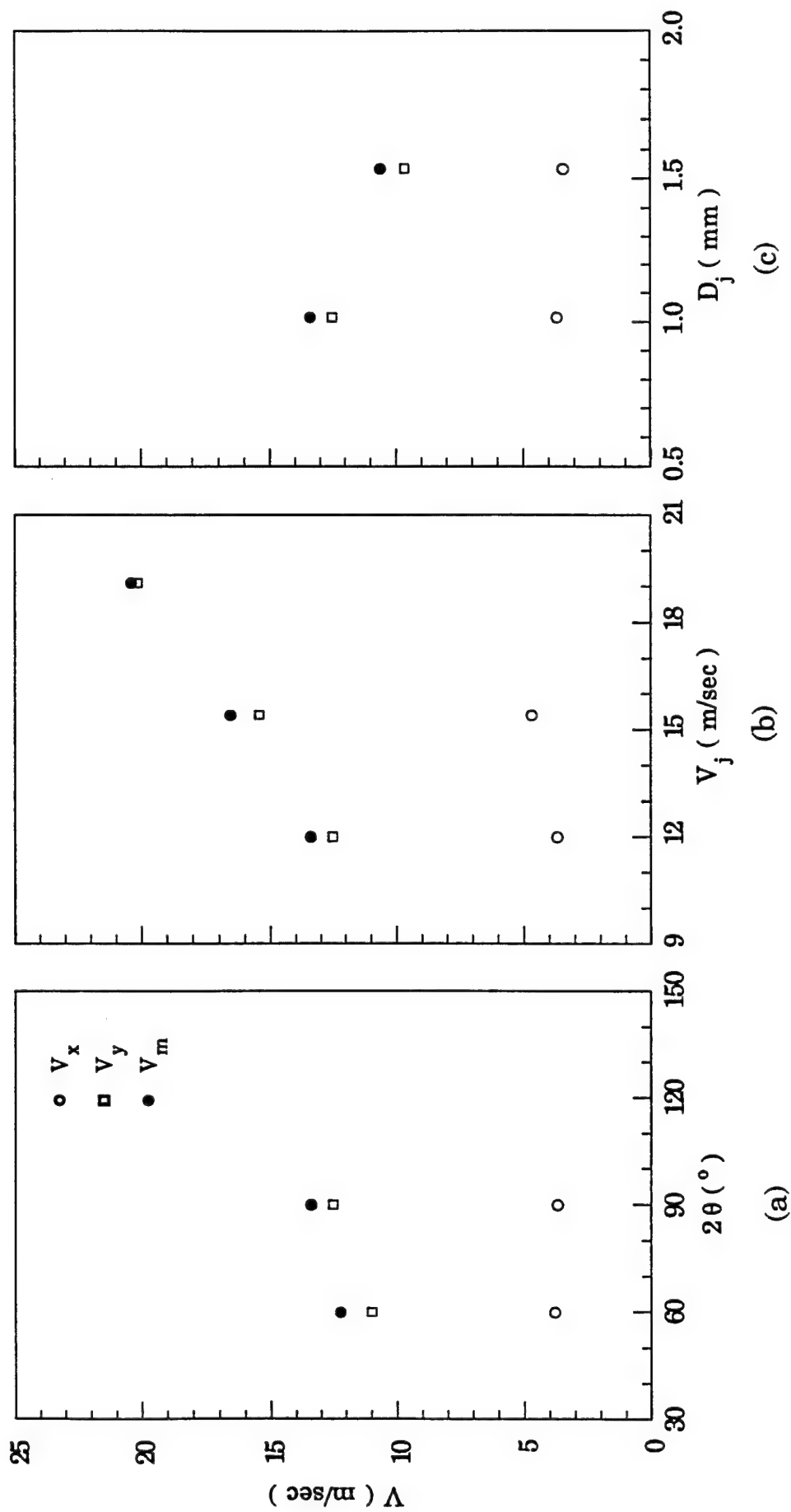


Figure 9 Effect of impingement angle, liquid jet velocity, and orifice diameter on mean droplet velocity (a)  $D_j = 1.0$  mm,  $V_j = 12.0$  m/s (b)  $D_j = 1.0$  mm,  $2\theta = 90^\circ$  (c)  $V_j = 12.0$  m/s,  $2\theta = 90^\circ$ .

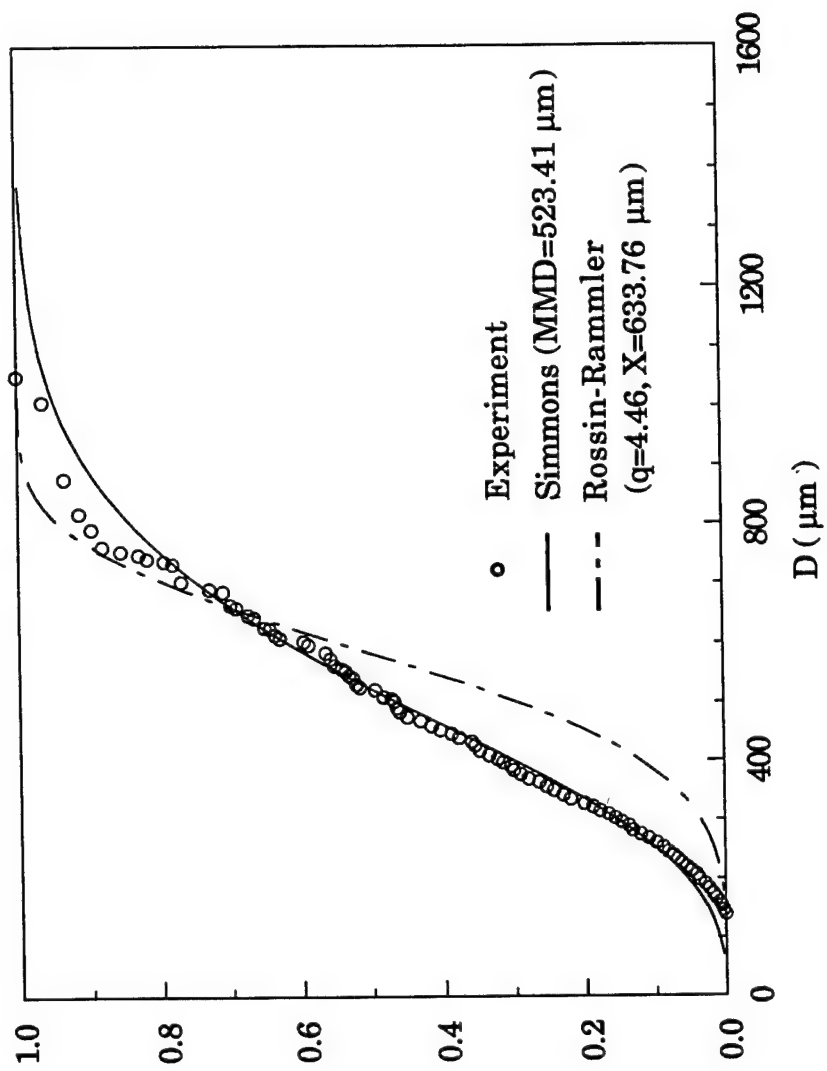


Figure 10 Cumulative volume distribution for  $D_j=1.0$  mm,  $V_j=12.0$  m/s,  $2\theta=90^\circ$



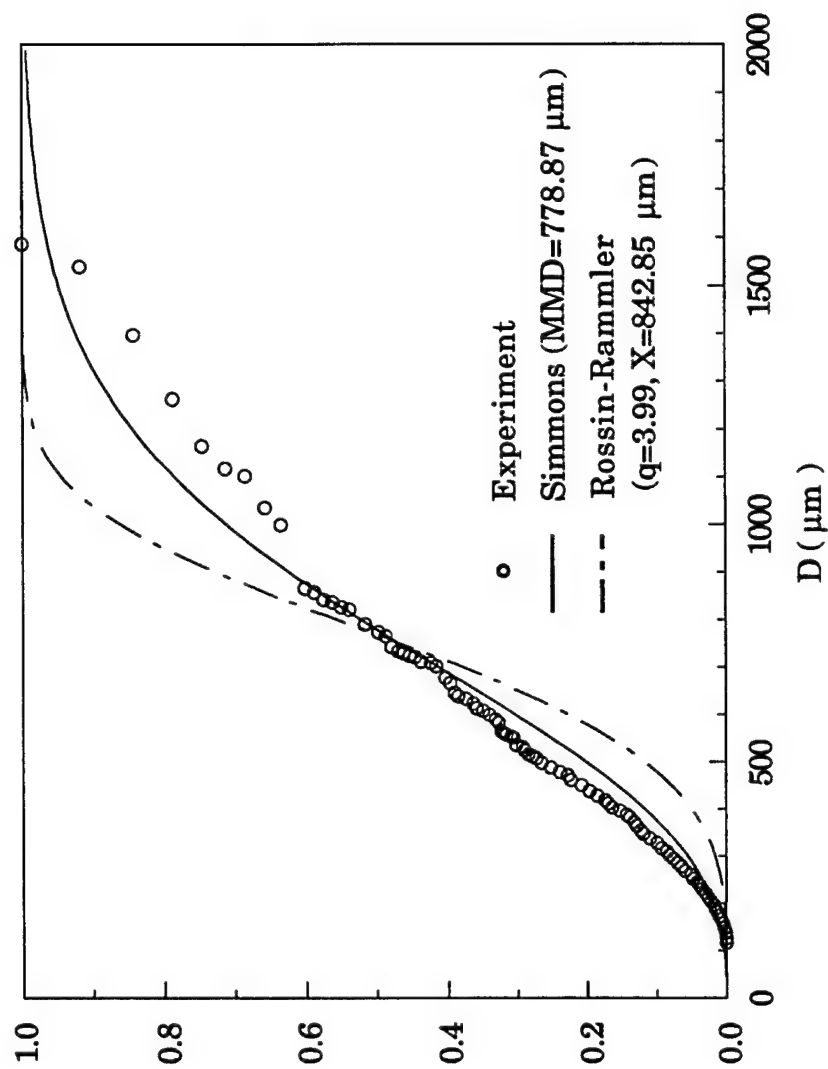


Figure 11 Cumulative volume distribution for  $D_j=1.0$  mm,  $V_j=12.0$  m/s,  $2\theta=60^\circ$

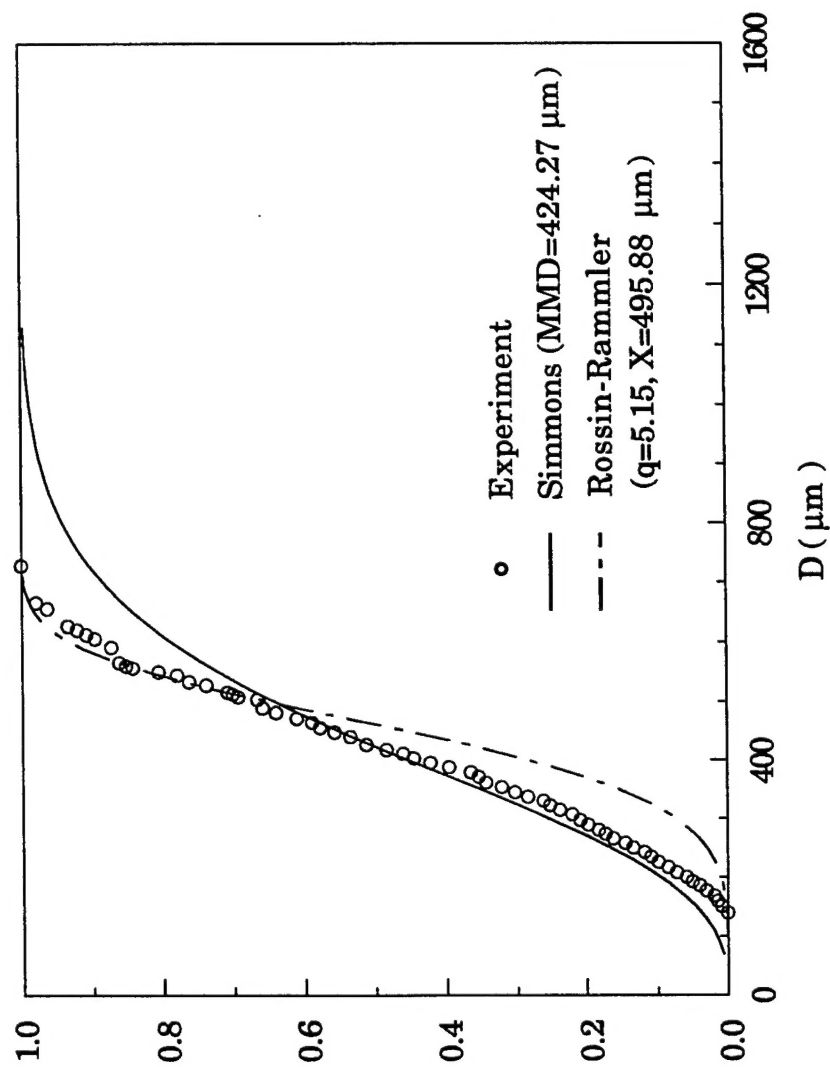


Figure 12 Cumulative volume distribution for  $D_j=1.0$  mm,  $V_j=12.0$  m/s,  $2\theta=120^\circ$

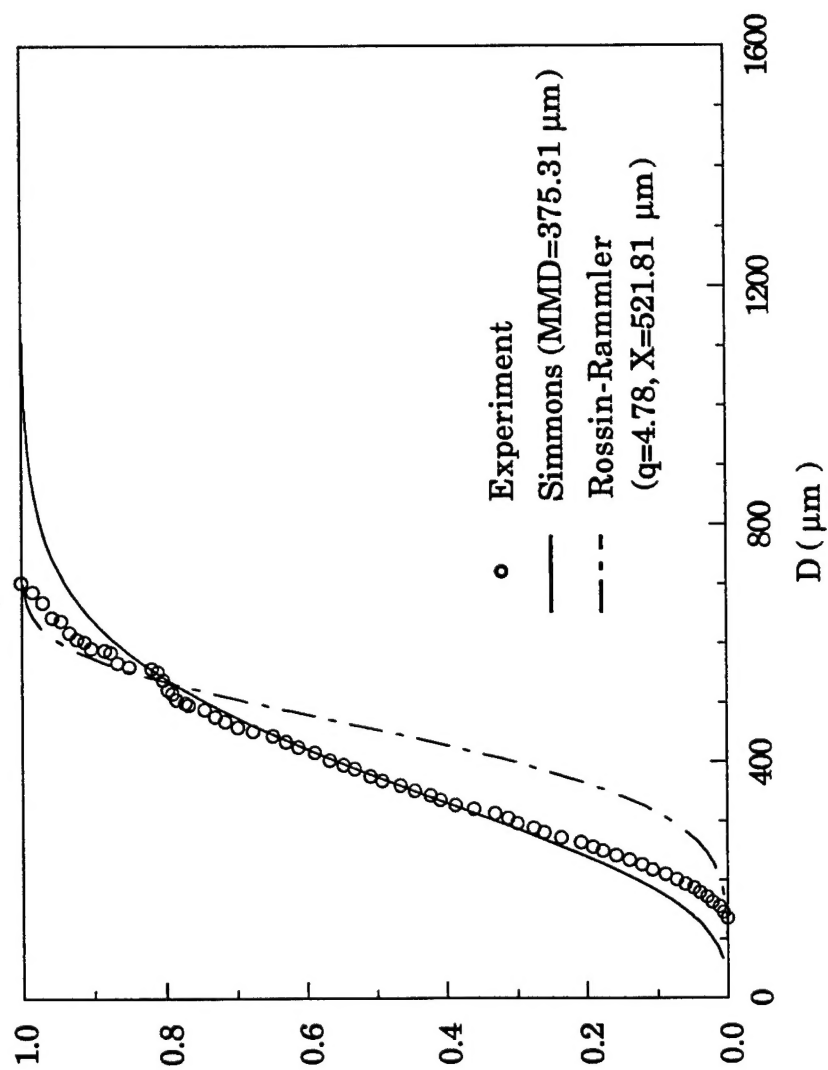


Figure 13 Cumulative volume distribution for  $D_j=1.0$  mm,  $V_j=15.4$  m/s,  $2\theta=90^\circ$

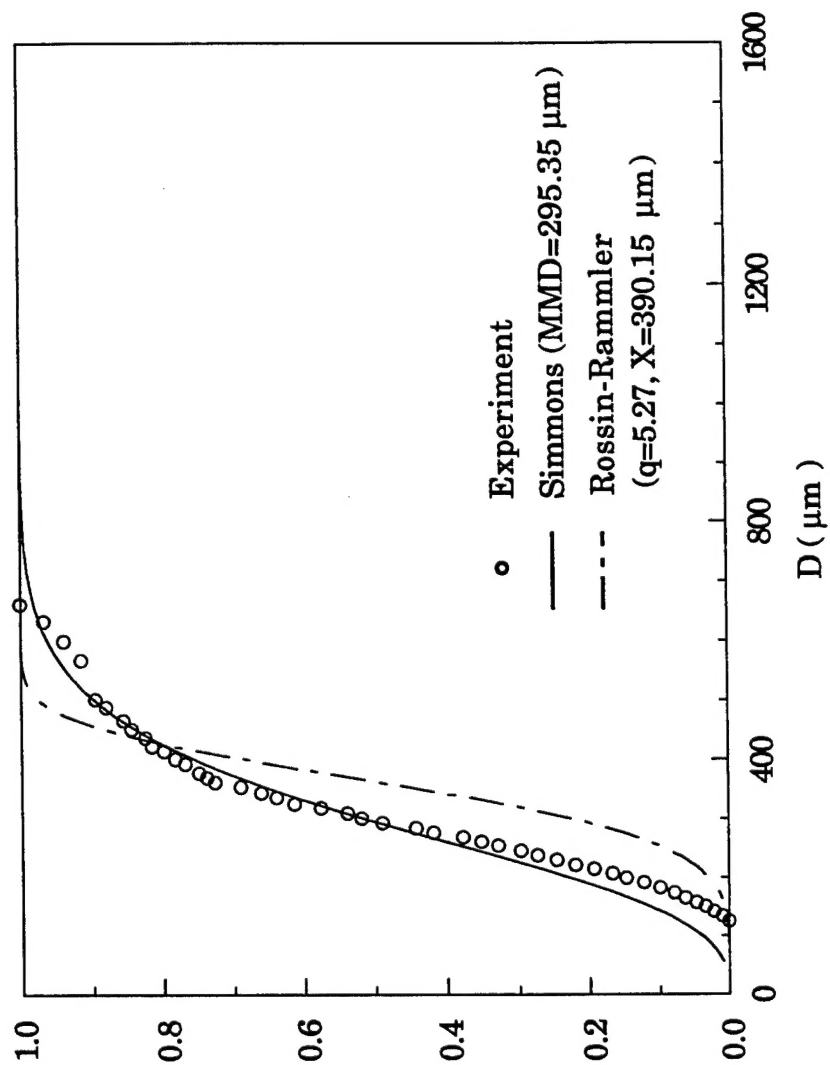


Figure 14 Cumulative volume distribution for  $D_j=1.0$  mm,  $V_j=19.1$  m/s,  $2\theta=90^\circ$

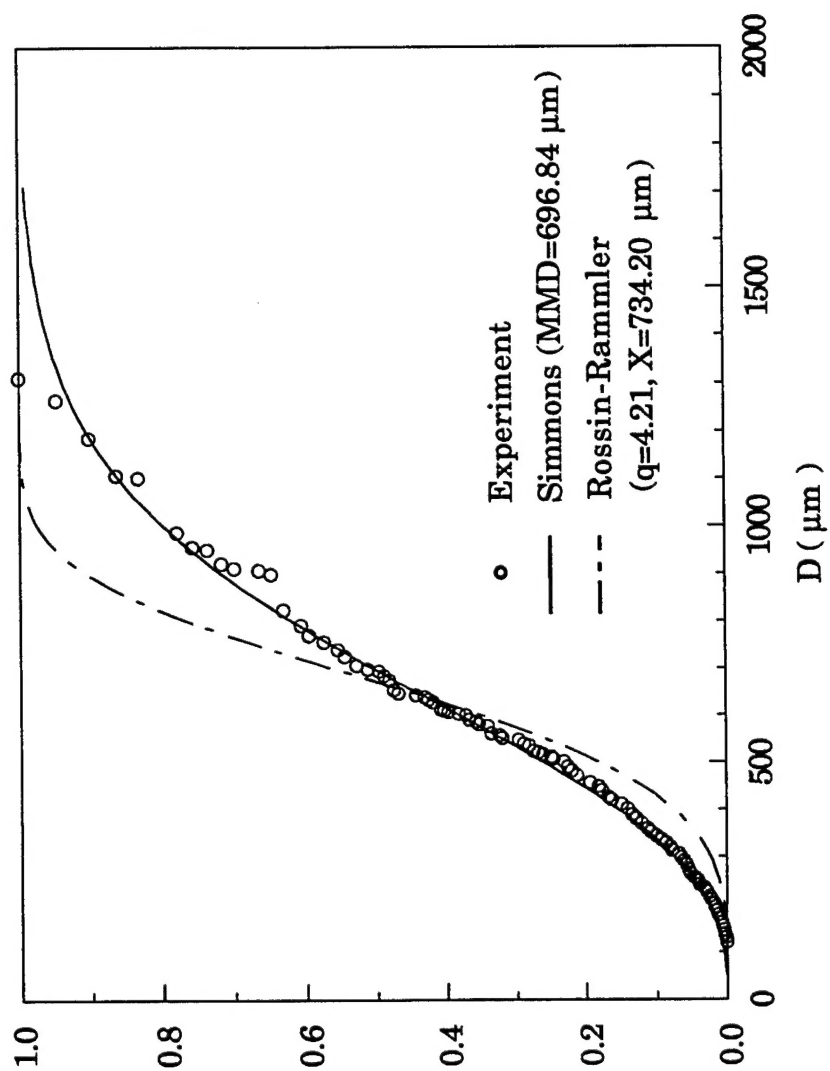


Figure 15 Cumulative volume distribution for  $D_j=1.5 \text{ mm}$ ,  $V_j=12.0 \text{ m/s}$ ,  $2\theta=90^\circ$